

## RESEARCH ARTICLE

10.1029/2018JA025501

## Key Points:

- The ability of the GOLD instrument to observe gravity wave fluctuations is examined
- A 10% perturbation in temperature and densities resulted in a change in brightness in FUV emissions observed from geostationary orbit
- Signal integration, on the order of minutes, would allow observations of perturbations due to gravity waves

## Correspondence to:

K. R. Greer,  
katelynn.greer@iasp.colorado.edu

## Citation:

Greer, K. R., England, S. L., Becker, E., Rusch, D., & Eastes, R. (2018). Modeled gravity wave-like perturbations in the brightness of far ultraviolet emissions for the GOLD mission. *Journal of Geophysical Research: Space Physics*, 123. <https://doi.org/10.1029/2018JA025501>

Received 6 APR 2018

Accepted 7 JUN 2018

Accepted article online 19 JUN 2018

## Modeled Gravity Wave-Like Perturbations in the Brightness of Far Ultraviolet Emissions for the GOLD Mission

K. R. Greer<sup>1</sup> , S. L. England<sup>2</sup> , E. Becker<sup>3</sup> , D. Rusch<sup>1</sup>, and R. Eastes<sup>1</sup> 

<sup>1</sup>University of Colorado Boulder-LASP, Boulder, CO, USA, <sup>2</sup>Virginia Polytechnic Institute and State University, Blacksburg, VA, USA, <sup>3</sup>Leibniz Institute of Atmospheric Physics, Kühlungsborn, Germany

**Abstract** The NASA Global-scale Observations of Limb and Disk (GOLD) mission will study the coupling of the thermosphere with the lower atmosphere through an examination of temperature and composition, allowing the study of atmospheric waves. A key mechanism of energy and momentum transport between atmospheric regions is gravity waves. GOLD is an imaging spectrograph that will measure Earth's airglow emissions (both nightglow and dayglow) in the far ultraviolet range from 132 to 162 nm, including the atomic oxygen doublet at 135.6 nm and molecular nitrogen Lyman-Birge-Hopfield bands. GOLD will be the first instrument to make such measurements from the perspective of a geostationary orbit, which creates unique challenges and opportunities for observing atmospheric waves. Here we model the ability of the GOLD imager to detect a gravity wave-like perturbation from the emergent brightness variations using a combination of a general circulation model and a model of the thermospheric airglow in the far ultraviolet. A 10% perturbation in temperature ( $\pm 59$  K at 150 km) and constituent densities is introduced into the vertical columns of the atmosphere, which results in a  $\pm 1.5$  Rayleigh perturbation to the brightness of both spectral features, with the same wave period as the introduced perturbation. For the expected total signal, particle background counts, and chosen spectral feature, signal-to-noise calculations indicate that integration for several minutes will allow gravity wave perturbations to be observed in brightness perturbations on a single pixel of an image.

**Plain Language Summary** The NASA Global-scale Observations of Limb and Disk (GOLD) mission will study how the thermosphere is connected to the lower and middle atmosphere by atmospheric waves. Of key interest are atmospheric gravity waves. These waves transfer energy and momentum between different atmospheric regions and have the ability to alter the temperature, composition, and winds of the upper atmosphere. In this study, we create a simple representation of a gravity wave-like structure and model such waves that would impact the emissions from Earth's atmosphere at two of the wavelengths observed by the GOLD instrument. It is found that the GOLD instrument will be able to observe a periodic change in observed brightness related to the gravity wave-like structure but will require summing the signal taken over a period of several minutes in order to distinguish waves of 10% in the temperature and densities.

## 1. Introduction

Gravity waves play a key role in energy and momentum transfers throughout the atmosphere, thereby exerting a strong dynamical control on the mean state and variability of the middle and upper atmosphere (Fritts et al., 2006; Fritts & Alexander, 2003; Smith, 2012). They are also understood to be ubiquitous (Forbes et al., 2016; Yiğit & Medvedev, 2010). As gravity waves propagate vertically, they grow in amplitude until they dissipate from dynamical instability (including critical levels) and turbulence, or directly from molecular viscosity. While the former process is typical for the middle atmosphere, the latter applies to the thermosphere.

Gravity waves propagating into the middle atmosphere typically originate in the lower atmosphere. The sources of these "primary" gravity waves include orography, deep convection, and jets/fronts (Fritts & Alexander, 2003; Plougonven & Zhang, 2014). Gravity waves in the upper atmosphere can still be primary waves (Vadas & Fritts, 2006; Vadas, 2013). In addition, there is evidence that gravity waves observed in the upper mesosphere and in the thermosphere are also generated from the body forces that result from the dissipation of the primary gravity waves (Vadas, 2007; Vadas et al., 2003, 2018). These gravity waves have large scales and high horizontal phase speeds; they can induce traveling ionospheric disturbances (Francis, 1973; Richmond, 1978; Vadas & Nicolls, 2009; Vlasov et al., 2011). Gravity waves from a mix of sources may be observable by Global-scale Observations of Limb and Disk (GOLD), and their analysis may lead to new insight into the vertical coupling process related to primary and secondary gravity waves.

Observations of gravity waves in the middle and upper thermosphere are still limited and sparse. Several papers (e.g., Bruinsma & Forbes, 2008; Park et al., 2014) have analyzed gravity waves observed by the Challenging Minisatellite Payload (CHAMP) near 300–400 km in altitude. Data from the Gravity Field and Steady-State Ocean Circulation Explorer (GOCE) mission, near 270 km, allowed Garcia et al. (2016) to create a climatology of gravity waves based on solar flux conditions. However, as these are moving platforms making in situ measurements, the derived horizontal wavelengths are not definitive and the gravity wave periods cannot be estimated (Garcia et al., 2016).

Given the dearth of observations of gravity waves in the thermosphere, modeling of gravity waves has been undertaken by several groups over the last decade. The response of both the ionosphere and thermosphere to gravity waves excited by deep convective plumes using a combination of a general circulation model (GCM), a convective plume model, and ray tracing was studied by Vadas and Liu (2009). Using a GCM with gravity wave parameterization, Yiğit and Medvedev (2010) studied the dynamical and thermal effects of gravity waves in the thermosphere under varied solar parameters. While some high-resolution GCMs extending into thermosphere resolve gravity waves in the lower and middle atmosphere (Liu, 2017; Liu et al., 2014; Watanabe & Miyahara, 2009), the waves are usually strongly damped above the mesopause by artificial hyperdiffusion and Rayleigh friction in these models. Recently, Becker and Vadas (2018) used a gravity wave resolving version of the Kühlungsborn mechanistic circulation model (KMCM) to interpret lidar observation by Chen et al. (2016) which showed persistent large-amplitude gravity waves in the mesopause region over Antarctica during wintertime. A different sort of model, the transfer function model, has been used to look at gravity waves effects on composition in the thermosphere (Mayr et al., 2013). Using a full wave model, Hickey et al. (2015) showed that in a binary gas thermosphere, viscosity and thermal conduction impact individual species' relative perturbations. While these complex and coupled models capture a range of the multifaceted behavior of gravity waves, simpler models may be suitable for examining the ability of new instruments to observe gravity waves.

The GOLD instrument was launched aboard the SES-14 communications satellite on 25 January 2018, and it is expected to begin observation operations in October of 2018. The mission will be located in a geostationary orbit over 47.5°W longitude. The instrument is a far ultraviolet (FUV) imaging spectrograph, the observations from which can be used to derive thermospheric temperature and composition as well as equatorial ionospheric structure. GOLD will make scans of the disk, creating disk images of atomic oxygen 135.6-nm emissions and molecular nitrogen Lyman-Birge-Hopfield (LBH) emissions every 30 min (Eastes et al., 2017). GOLD will have a nadir-viewing observation footprint of 50 km × 40 km from its high resolution slit and 100 km × 40 km from its medium resolution slit. One of the specific science questions to be addressed by the mission concerns the impact of atmospheric waves propagating up from below on the thermosphere. Of particular interest are thermospheric gravity waves given their limited observations and the importance of the multistep vertical coupling process associated with these waves. Because of its unique viewing geometry, it is expected that GOLD will be able to retrieve the horizontal wavelengths and the periods of gravity waves. Campaign modes may allow the slit of the imager to be “parked” and stare at a region of interest on the Earth (such as a gravity wave “hot spot”) for extended periods of time. Previous missions that observed thermospheric gravity waves in situ (such as CHAMP and GOCE) could only estimate the horizontal wavelength because of their moving platform (Garcia et al., 2016). While the derived quantities of temperature and O/N<sub>2</sub> can be used to determine wave characteristics, it may be desirable to use gravity wave perturbations in the emission rates as a proxy for their characteristics; as such, signals are inherently more robust to the effects of noise than derived quantities such as thermospheric temperature.

In this paper, we use the Global Airglow (GLOW) model to simulate the observations of gravity wave-like disturbances by the GOLD mission in the 135.6 nm and LBH emissions. The background atmosphere is given by the thermosphere-ionosphere-electrodynamics GCM (TIEGCM), and a simple sine wave perturbation enclosed within a Gaussian envelope is imposed on the vertical columns of the atmosphere. In addition, we will use thermospheric gravity perturbations simulated with a high model-top version of the KMCM. As the GOLD instrument stares at a longitude-latitude location on the Earth, this perturbation may be observed as a periodic change in brightness corresponding to the period of the disturbance.

The paper is organized as follows: The models and methods are described in section 2. Results from the modeling experiment and potential mechanisms are discussed in section 3. Conclusions are given in section 4.

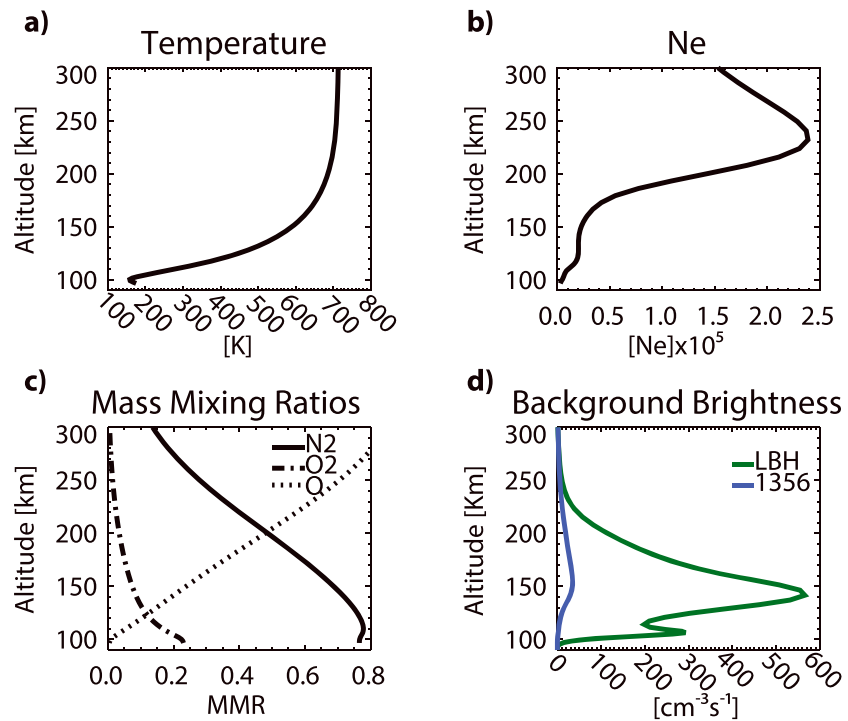


**Figure 1.** Output from TIEGCM for 21 June 2002 at 15:30 UT at the location of 47.5 W, 0 N. Shown in the panels are profiles of (a) temperature; (b) electron density; (c) mass mixing ratios of the major constituents of molecular nitrogen, molecular oxygen, and atomic oxygen; and (d) the volume emission rate [photons  $\text{cm}^{-3} \text{s}^{-1}$ ] for the Lyman-Birge-Hopfield bands and 135.6-nm features (from GLOW).

## 2. Methodology

Three models are used in this study. The GLOW model calculates the emission features in the FUV that the GOLD instrument is sensitive to for a given atmosphere. The atmosphere is modeled by the TIEGCM and outputs the neutral temperature, constituent gas mass mixing ratios, and ambient ionosphere electron density, electron temperature, and ion temperature. Gravity perturbations are superposed on the background atmosphere given by TIEGCM using simple analytical expressions. The KMCM helps guide the selection of the gravity wave characteristics.

### 2.1. TIEGCM

The TIEGCM is a global numerical model of Earth's upper atmosphere that includes the dynamics, energetics, and chemistry with a steady state ionospheric electrodynamic in a geomagnetic field defined by the International Geomagnetic Reference Field (Thébault et al., 2015). Here we use the TIEGCM-Ionospheric Connections Explorer version based on TIEGCM v2.0, which was developed in support of the Ionospheric Connections Explorer (ICON) mission and described more thoroughly by Maute (2017). It spans from 97 km to approximately 450 to 600 km, depending on solar cycle. The horizontal resolution is  $2.5^\circ$  longitude by  $2.5^\circ$  latitude and a vertical resolution of 1/4 scale height. TIEGCM incorporates upward propagating waves by specifying the tidal perturbations at the lower boundary, which are defined in terms of geopotential height, neutral temperature, and horizontal winds using HWM07 (Drob et al., 2008). The model was run under solar minimum and geomagnetically quiet conditions, where the  $f_{10.7}$  was 70 solar flux units. The model run was for 21 June 2002, and the state of the atmosphere was sampled at 10-min intervals. Profiles from this model run at 15:30 UT at  $47.5^\circ\text{W}$  and  $0^\circ\text{N}$  are shown in Figure 1. The temperature profile is shown in (a), the electron density is shown in (b), and the mass mixing ratios of major constituents are shown in (c). Also shown are the volume emission rates (photons  $\text{cm}^{-3} \text{s}^{-1}$ ) from GLOW for the LBH and 135.6 spectral features. The temperature rapidly climbs from the mesopause to the middle thermosphere, with a temperature of 588 K at 150 km, near the peak of the LBH and 135.6-nm emissions rates. The electron density shows

peaks in the *E* region and *F* region ionosphere. The mass mixing ratios illustrate the decreasing  $N_2$  and  $O_2$  with altitude while O increases.

## 2.2. KMCM

The KMCM is a free-running high-resolution atmospheric GCM that extends from the surface to the lower thermosphere. It is based on a standard spectral dynamical core with a terrain-following vertical coordinate and a staggered vertical grid according to Simmons and Burridge (1981). The spectral resolution (T240) corresponds to a grid-spacing of 55 km. The vertical level spacing is  $\sim 600$  m between the boundary layer and  $\sim 100$  km and increases in the lower thermosphere. In the standard model version (Becker & Vadas, 2018) we use 190 full levels with a model top at  $\sim 135$  km. For the interpretation of data expected from the GOLD mission, a high-model-top version with 220 pressure levels and a model top at  $\sim 200$  km is available. The KMCM includes simplified but nevertheless explicit representations of the relevant components of a climate model: radiative transfer, water vapor transport and moist convection, the full surface energy budget, as well as simple representation of processes relevant in the thermosphere. These methods are described in Becker et al. (2015) and Becker (2017). The current high-resolution version of the KMCM does not include GW parameterization. Except for moist convection, subgrid scales are solely parameterized in terms of (macro-)turbulent nonlinear diffusion (Becker, 2009). Linear (harmonic) diffusion is employed in the upper most model layers to prevent wave reflection from the model top. This sponge layer is less important in the high-model-top version since ion drag efficiently dissipates wave energy above  $\sim 150$  km. The complete momentum diffusion is based on a symmetric stress tensor formulation and preserves angular momentum. All subgrid-scale parameterizations fulfill the energy conservation law. Summarizing, the GW resolving KMCM with the model top extended to 200 km is a GCM that explicitly simulates GWs from the surface up to altitudes of about 170 km.

## 2.3. GLOW

The GLOW model simulates observable emissions of the upper atmosphere. GLOW is a 1-D model that can be run repeatedly over a grid of longitudes and latitudes or time. It has a nominal altitude range of 80 km to approximately 600 km. Required inputs include neutral temperature  $T_N$ ; the mass mixing ratios of  $N_2$ ,  $O_2$ , O, NO, and ground state atomic Nitrogen  $N(^4S)$ ; electron number density  $N_e$ ; electron temperature  $T_{e_i}$ ; and ion temperature  $T_i$ . The outputs of ionized/excited species densities and airglow emissions rates are produced from internal calculations of ionization, dissociation, excitation rates, energetic electron transport, and ion-neutral chemistry. It has recently been updated to include emissions in the FUV, including the LBH bands of molecular nitrogen and the atomic doublet at 135.6 nm (Solomon, 2017) that will be observed by the GOLD mission. Postprocessing algorithms are available to account for the radiative transfer effects for the 135.6-nm emission and absorption by  $O_2$  for the LBH emission. GLOW is currently configured to use MSIS as the specified atmosphere or the output of TIEGCM. When TIEGCM is the input to GLOW, GLOW has the same spatial resolution as its input. Please see Solomon (2017) and references there-in for more details and postprocessing tools. Model codes are freely available at the HAO/NCAR website <https://www2.hao.ucar.edu>.

Figure 2 shows the GLOW modeled LBH and 135.6-nm brightness as viewed from geostationary orbit at  $47.5^\circ W$  longitude for 21 June 2002 at 15.5 UT based on TIEGCM inputs. Postprocessing accounts for absorption by  $O_2$  and observational geometry including limb and disk viewing.

## 2.4. Synthetic Perturbation to Simulate Gravity Wave Impacts on Airglow

As TIEGCM does not resolve small-scale gravity waves, a gravity wave-like perturbation is introduced to the vertical columns of the atmosphere as shown in Figure 3. The perturbation is a sinusoidal wave with a period of 1 hr, enclosed within a Gaussian envelope. We use percent change in temperature to display this as the background temperature and density are rapidly changing with altitude (see Figure 1). We selected an amplitude of perturbation that maximizes as a 10% change in temperature and in densities (with a phase shift of  $180^\circ$ ) at 150 km. At 150 km (near the peak in emission from LBH and 135.6-nm features), this corresponds to a  $\pm 59$  K variation. Since there are relatively few observations or modeling studies of this region, comparisons of this amplitude with other work are scarce. Our perturbations are somewhat smaller than those used by Hickey et al. (2015) and in line with the relative perturbations found by Chen et al. (2016) Becker and Vadas (2018) for the 90–110 km altitude ranges.

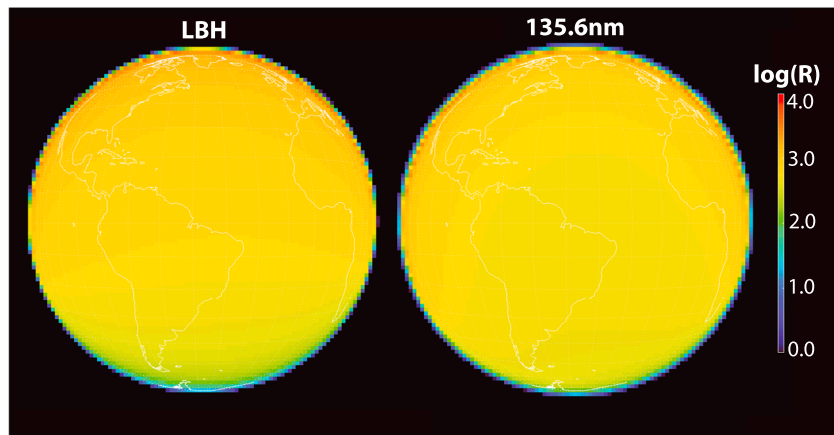


**Figure 2.** Brightness in the Lyman-Birge-Hopfield and 135.6-nm emissions in Rayleighs produced by GLOW as viewed from geostationary orbit at 47.5 W longitude for 21 June 2002 at 15:30 UT, using the unperturbed TIECM inputs.

The perturbation is introduced into every vertical column in the TIEGCM background atmosphere, but there is no longitudinal or latitudinal structure. In the real atmosphere, gravity waves are complex 3-dimensional structures. While this methodology misses some of the intrinsic complexity of gravity waves, it nevertheless allows an examination of the temporal variability of brightness that may be observed by a GOLD-like instrument dwelling over a single geographic point. This perturbation was applied to neutral temperature, electron temperature, and ion temperature. A perturbation that is 180° out of phase with the temperature perturbation was also applied to O<sub>2</sub> and N<sub>2</sub>. In 2015, Hickey et al. conducted a gravity wave experiment with a binary gas model of the thermosphere where they found that in the lower thermosphere N<sub>2</sub> oscillates antiphase to the lighter O due to differential advection. We follow those results and apply a perturbation to O that is antiphase to N<sub>2</sub>. The volume emission rates are then calculated by GLOW.

### 3. Results and Discussion

After the volume emission rates are calculated by GLOW for the desired spectral features, postprocessing is done to obtain column or slant column brightness. The brightness that emerges from the atmosphere and is captured by an instrument at geostationary orbit is not simply the vertically integrated column of volume emission rates. The viewing geometry requires that the integration be done along the line of sight, so the only column that will be vertically integrated is the column in the nadir direction. Off-nadir directions are slant columns. Only disk information is examined; results from limb calculations are not considered here.

Further, if the emission is subjected to partial absorption, this must be considered by calculating the slant column density and then applying Beer's law. The N<sub>2</sub> LBH bands and the O(<sup>5</sup>S) doublet at 135.6 nm are subject to absorption by O<sub>2</sub>, and this is accounted for in the following results.

Figure 4 shows the change in brightness emerging from atmosphere as observed from geostationary orbit for (a) LBH and (b) the 135.6 nm O(<sup>5</sup>S) spectral features as modeled by GLOW viewed in the nadir direction. The background, which changes with time as the solar zenith angle changes, is fit with a least squares fits of four sinusoidal functions and removed. After this background removal, a clear periodic signal is seen with a 1-hr period that matches the input perturbation in both LBH and 135.6 nm, indicating that this is a potentially valid method for studying middle thermospheric gravity waves. The resulting brightness perturbation is about ±1.5 Rayleigh for the input 10% change in temperatures and densities.

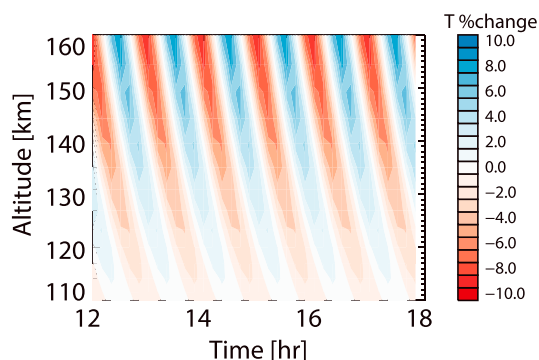


**Figure 3.** Gravity wave-like perturbation in temperature introduced into the background TIEGCM atmosphere.

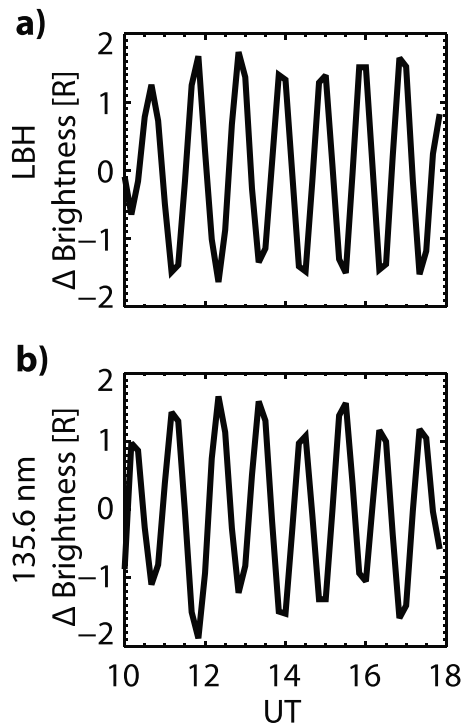


**Figure 4.** Brightness emerging from atmosphere as observed from geostationary orbit for (a) the Lyman-Birge-Hopfield and (b) 135.6-nm O(<sup>5</sup>S) spectral features.

While the 1-hr period wave used in this modeling experiment shows promise in retrieval of a gravity wave-like period, there are few observations of this region to guide the selection of gravity wave periods, vertical wavelengths, and amplitudes. Therefore, we analyze also results of gravity wave perturbations simulated by the KMCM with a model top at 200 km. Figure 5 shows an example of gravity wave perturbations in temperature from the KMCM, using a running mean of 4 hr as the background state. The data shown are from the area downstream of the main gravity wave hot spot in the southern hemisphere (off the southeast coast of South America at 48°W and 45°S). Figure 5 contains a dominant gravity wave period of approximately 3 hr near 150 km with a temperature amplitude of about 10%. The overall structure is more complex and cannot be approximated by a monochromatic wave. The reason is that the gravity wave spectrum evolves with altitude due to molecular viscosity and thermal diffusivity such that gravity waves with longer vertical wavelengths and shorter intrinsic periods prevail at greater heights in the thermosphere (Vadas, 2007; Vadas & Fritts, 2005). This effect is also reflected by the temperature perturbation extracted from the KMCM.

In order keep the simplicity of our brightness calculations when using gravity wave parameters from the KMCM, we apply a synthetic perturbation that matches with the dominant gravity wave period and vertical wavelength that is seen in the KMCM data at 150 km, and the results are shown in Figure 6. Figure 6a shows the 3-hr period perturbation applied to temperature (perturbations to O, O<sub>2</sub>, N<sub>2</sub>, and He density were also applied but not shown here); Figure 6b shows the change in brightness emerging from atmosphere the as observed

from geostationary orbit for LBH and Figure 6c the O(<sup>5</sup>S) 135.6-nm spectral features. The 3-hr gravity wave period is again reflected in brightness oscillation. The solid line is nadir viewing, while the dashed line is for a line-of-sight observation 4° off of nadir (from an instrument at geostationary orbit) in the +x (east) direction (near 25°W longitude). As the off-nadir line of sight slant path is longer than the nadir vertical path, the amplitude of the off-nadir wave is increased because this longer path contains additional photons. For the off-nadir slant path, the horizontal structure of the waves must be considered in interpreting actual observations (Belyaev, 2009; Preusse et al., 2002), possibly limiting observations to longer horizontal wavelengths.

Since gravity wave-like perturbations fulfill the anelastic approximation (e.g., appendix in Becker, 2017), the associated relative temperature and density changes are out of phase by 180°. Hence, if a gravity wave passes through a column of air, the emergent brightness is a combination of the associated temperature and density perturbations. Upon examination of Figures 6b and 6c, it is evident that signals from LBH and 135.6 nm are out of phase. This suggests that the density/composition changes are mainly responsible for the changes in brightness. The LBH bands, which are produced by N<sub>2</sub>, were perturbed by the density. The O perturbation, which is responsible for the 135.6-nm feature, was imposed to be in antiphase to N<sub>2</sub>. Even though both constituents are affected by the same temperature, the antiphase relationship of their respective densities controls the phase relationship of the emergent brightness signals.

Given that the change in brightness for these gravity wave-like perturbations is approximately 1 Rayleigh, we now turn to how the GOLD instrument would be able to observe this change. Using ground-based calibration information and the equation for signal-to-noise ratio (SNR), we find that by using a campaign mode where GOLD “parks” one of its

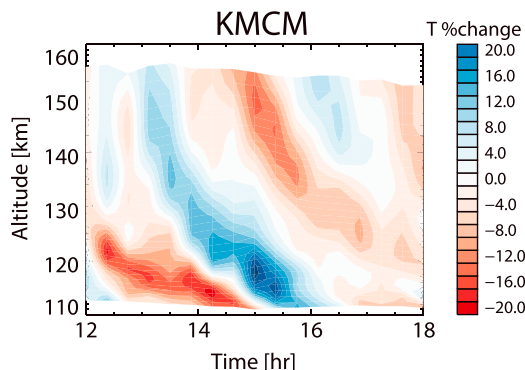


**Figure 5.** Gravity wave perturbation in percent change in temperature from Kühlungsborn Mechanistic general Circulation Model.

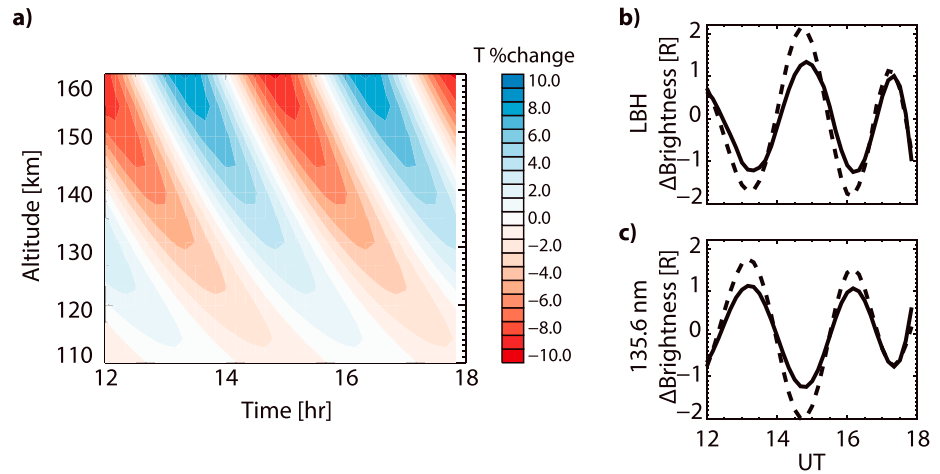


**Figure 6.** (a) The 3-hr perturbation as a percent change in temperature; the change in brightness emerging from atmosphere the as observed from geostationary orbit for (b) Lyman-Birge-Hopfield and (c) the O(<sup>5</sup>S) spectral features. The solid line is nadir viewing, while the dashed line is for a line-of-sight observation 4° off of nadir in the +x (east) direction.

slits over a geographic location, it will be able to integrate enough signal to observe these periodic changes in brightness. The SNR is calculated as

$$SNR = \frac{S \cdot R \cdot t}{\sqrt{S \cdot R \cdot t + B \cdot t}}$$

where  $S$  is the sensitivity of the detector,  $R$  is the total signal,  $t$  is time, and  $B$  is the background particle counts. The measured sensitivity for the O 135.6-nm portion of the detector that observes a  $50 \times 40 \text{ km}^2$  footprint with the high resolution slit (Eastes et al., 2017) is  $S_O = 5.1 \times 10^{-2} \text{ counts Rayleigh}^{-1} \text{ s}^{-1}$ , while  $S_{LBH} = 3.5 \times 10^{-2} \text{ counts Rayleigh}^{-1} \text{ s}^{-1}$ . The low resolution slit, which is twice as wide and doubles the signal levels, also provides the spectral resolution needed for observations of emission brightness but with better signal to noise. The total signal (see Figure 2, for example) expected, based on previous observations (Strickland et al., 2004) by GUVI, is over 500 Rayleighs of O 135.6 nm or N<sub>2</sub> LBH at solar zenith angles <70° during nominal conditions. The background noise on the detector is mostly due to gamma rays impacting the detector; models of this at geostationary orbit are variable but suggest a range of  $P = 50$  (median) to 270 (90th percentile) counts  $\text{cm}^{-2} \text{ s}^{-1}$ . The pixel area containing the 135.6-nm signal is

$A_O = 2.21 \times 10^{-3} \text{ cm}^2$ , while the pixel area containing the LBH area is  $A_{LBH} = 3.31 \times 10^{-2} \text{ cm}^2$ . The particle background for O is then  $B_O = A_O \cdot P$ . When using the low resolution slit, the pixel area increases by only a factor of ~1.5 because the contribution from optical aberrations does not increase with the slit width.

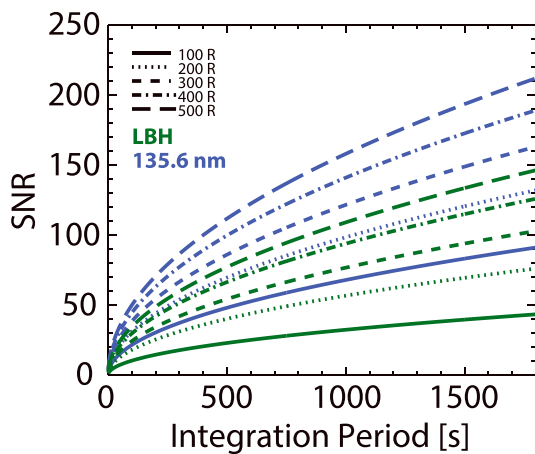


**Figure 7.** Signal-to-noise for both Lyman-Birge-Hopfield and 135.6-nm spectral features on the Global-scale Observations of Limb and Disk instrument for variable integration periods [s] and selected total signals [R]. The background count is set to 250 counts  $\text{cm}^{-2} \text{ s}^{-1}$ .

Figure 7 shows the SNR for both LBH and 135.6-nm spectral features on the GOLD instrument for variable integration periods [s] and selected total signals [Rayleighs]. The background count,  $P$ , is set to 250 counts  $\text{cm}^{-2} \text{ s}^{-1}$ , which is higher than the median background from radiation or that from scattering within the instrument of the Lyman alpha 121.6 nm and oxygen 130.4-nm emission. The combined signal from scattering of those emissions is expected to be less than the median background from radiation.

The LBH SNR is expected to be lower. Even though LBH is a brighter feature, its larger area on the detector means that the particle background is higher. To achieve a SNR of 100 for a signal of 500 R (which is slightly less than the anticipated LBH signal when observing at 70° solar zenith angle during solar minimum; Strickland et al., 2004) and background count of 250, it would be necessary to integrate for 841 s

for LBH and 400 s for 135.6 nm when using the narrow slit. Using the medium slit would reduce these times to approximately 600 and 290 s, respectively. In practice, imaging a more limited spatial region, rather than the full disk, would increase the probability of observing gravity waves. The parameters for such an approach are summarized below.

The GOLD imager observes a rectangular area, corresponding to the spectrograph's entrance slit, along which it has spatial information at a resolution of  $\sim 40$  km, primarily in latitude. The space covered in the other dimension is  $\sim 50$  km when using the narrowest slit or  $\sim 100$  km when using the medium width slit, either of which can be used for observations for gravity waves. Spatial information (primarily) longitudinal direction, perpendicular to the longer dimension of the slit, is obtained by sweeping (scanning) the slit across the Earth. Since the angular range scanned is adjustable, it can be optimized for observing gravity waves. Since typical wavelengths for gravity waves are estimated to 300 to 1200 km with typical horizontal velocities of 80 m/s (Forbes et al., 2016; Vadas, 2007; Yiğit et al., 2008; Yiğit & Medvedev, 2015), it takes  $\sim 10$  min for wave to move across the  $\sim 50$  km covered by the narrow slit (propagating perpendicular to the slit length). Waves propagating across, rather than along, the slit are more likely and that orientation decreases the changes seen at locations along a stationary (not scanning) slit, decreasing the likelihood of their identification, especially if they are stationary. Therefore, scanning of a limited longitude range may increase the probability of observing gravity waves, although it decreases the SNR per unit area observed. The spatial coverage (in the longitude direction) should be sufficiently large to distinguish between the effects of the longest wavelength gravity waves and larger scale temporal variations (too narrow a region may have the same limitation as a fixed slit) and rapid enough to distinguish gravity waves crossing the region. Assuming a wavelength of 1,200 km, for which it is expected to be the most difficult to achieve sufficient SNR because greater spatial coverage is needed, it should be sufficient to cover 600 km (wavelength/2). This corresponds to 12 steps of 50 km by the narrowest slit or 6 steps of 100 km by the medium slit. Such an observing area should be large enough to allow distinguishing spatial variations produced by the wave (in one scene) from global scale changes. Assuming 600 km is covered, for 30 min of total observing time—which can be summed later without any addition of noise since the individual photon events are transmitted to the ground—divided equally between the steps, the SNR at 100 km  $\times$  100 km resolution (after summing the data) would be 120 with the narrow slit and 168 with the medium slit for the oxygen 135.6-nm emission.

While the wave may be retrieved from brightness changes in either the LBH or 135.6-nm spectral features, based on this SNR information, it will likely be better to use 135.6 nm since the integration period is shorter. Further, given the phase difference between O and N<sub>2</sub> in the gravity waves, it may also be valuable to perform a cross correlation in the signals to verify detected waves. Observing temperature perturbations produced by the wave depends on the LBH SNR alone. As calculated earlier (cf., Figure 7), the time required to achieve the same SNR (e.g., 100) using the LBH emissions is twice that of the oxygen 135.6-nm emission. Temperatures can be retrieved using observations taken with either the narrowest slit or the medium width slit. At a SNR of 100 the expected uncertainty in the temperatures retrieved is better than  $\pm 30$  K (Eastes et al., 2017) in a pixel. Consequently, gravity waves producing a 10% change in the temperatures ( $\sim 600$  K) near the peak ( $\sim 160$  km) of the N<sub>2</sub> emission are expected to be observable.

#### 4. Conclusions

In this paper, we analyze a simple gravity wave-like perturbation that may be observed in the upcoming GOLD mission using GLOW to model the emitted light from the LBH bands and atomic oxygen doublet at 135.6 nm. The background atmosphere was modeled using TIEGCM. The perturbation period imposed on temperature and constituent densities were retrieved from the emergent brightness for a GOLD-like instrument located at geostationary orbit. These brightness also depend on viewing geometry; off-nadir viewing results in a greater amplitude of perturbation brightness. A 10% perturbation in temperature and densities results in an approximately  $\pm 1$  Rayleigh change in emergent brightness for both spectral features, and the LBH and 135.6 brightness perturbations are out of phase. SNR calculations indicate that several minutes to tens of minutes of integration will be required to observe brightness changes at this level for a gravity wave-like perturbation, and perturbations are expected to be more readily observed in 135.6 nm than in LBH.

**Acknowledgments**

This work was supported by the National Aeronautics and Space Administration's Explorer Program through contract NNG19PQ28C to the University of Central Florida and subcontract 66016029-01 to the Laboratory of Atmospheric and Space Physics. We wish to thank Astrid Maute and the TIEGCM development team as well as Stan Solomon for valuable assistance with the GLOW code and postprocessing tools. Code for running TIEGCM is freely available at <http://www.hao.ucar.edu/modeling/tgcm>. Code for running GLOW is freely available at <https://www2.hao.ucar.edu/modeling/glow>. We thank Sharon L. Vadas for valuable discussions regarding thermospheric gravity waves and the development of the high-top version of the gravity wave resolving KMCM. The data shown in this paper are available for collaborative research on Open Science Framework at <https://osf.io/8hp7f/>.

**References**

Becker, E. (2009). Sensitivity of the upper mesosphere to the Lorenz energy cycle of the troposphere. *Journal of Atmospheric Science*, 66(3), 647–666. <https://doi.org/10.1175/2008JAS2735.1>

Becker, E. (2017). Mean-flow effects of thermal tides in the mesosphere and lower thermosphere. *Journal of Atmospheric Science*, 74(6), 2043–2063. <https://doi.org/10.1175/JAS-D-16-0194.1>

Becker, E., Knöpfel, R., & Lübken, F.-J. (2015). Dynamically induced hemispheric differences in the seasonal cycle of the summer polar mesopause. *Journal of Atmospheric and Solar-Terrestrial Physics*, 129, 128–141. <https://doi.org/10.1016/j.jastp.2015.04.014>

Becker, E., & Vadas, S. L. (2018). Secondary gravity waves in the winter mesosphere: Results from a high-resolution global circulation model. *Journal of Geophysical Research: Atmospheres*, 123, 2605–2627. <https://doi.org/10.1002/2017JD027460>

Belyaev, A. N. (2009). An emission layer as a gravity wave detector. *Journal of Atmospheric and Solar-Terrestrial Physics*, 71(17–18), 1974–1981. <https://doi.org/10.1016/j.jastp.2009.09.001>

Bruinsma, S. L., & Forbes, J. M. (2008). Medium- to large-scale density variability as observed by CHAMP. *Space Weather*, 6, S08002. <https://doi.org/10.1029/2008SW000411>

Chen, C., Chu, X., Zhao, J., Roberts, B. R., Yu, Z., Fong, W., et al. (2016). Lidar observations of persistent gravity waves with periods of 3–10 h in the Antarctic middle and upper atmosphere at McMurdo (77.83°S, 166.67°E). *Journal of Geophysical Research: Space Physics*, 121, 1483–1502. <https://doi.org/10.1002/2015JA022127>

Drob, D. P., Emmert, J. T., Crowley, G., Picone, J. M., Shepherd, G. G., Skinner, W., et al. (2008). An empirical model of the Earth's horizontal wind fields: HWM07. *Journal of Geophysical Research*, 113, A12304. <https://doi.org/10.1029/2008JA013668>

Eastes, R. W., McClintock, W. E., Burns, A. G., Anderson, D. N., Andersson, L., Codrescu, M., et al. (2017). The Global-Scale Observations of the Limb and Disk (GOLD) mission. *Space Science Reviews*, 212(1–2), 383–408. <https://doi.org/10.1007/s11214-017-0392-2>

Forbes, J. M., Bruinsma, S. L., Doornbos, E., & Zhang, X. (2016). Gravity wave-induced variability of the middle thermosphere. *Journal of Geophysical Research: Space Physics*, 121, 6914–6923. <https://doi.org/10.1002/2016JA022923>

Francis, S. H. (1973). Acoustic-gravity modes and large-scale traveling ionospheric disturbances of a realistic, dissipative atmosphere. *Journal of Geophysical Research*, 78(13), 2278–2301. <https://doi.org/10.1029/JA078i013p02278>

Fritts, D. C., & Alexander, M. J. (2003). Gravity wave dynamics and effects in the middle atmosphere. *Reviews of Geophysics*, 41(1), 1003. <https://doi.org/10.1029/2001RG000106>

Fritts, D. C., Vadas, S. L., Wan, K., & Werne, J. A. (2006). Mean and variable forcing of the middle atmosphere by gravity waves. *Journal of Atmospheric and Solar-Terrestrial Physics*, 68(3–5), 247–265. <https://doi.org/10.1016/j.jastp.2005.04.010>

Garcia, R. F., Bruinsma, S., Massarweh, L., & Doornbos, E. (2016). Medium-scale gravity wave activity in the thermosphere inferred from GOCE data. *Journal of Geophysical Research: Space Physics*, 121, 8089–8102. <https://doi.org/10.1002/2016JA022797>

Hickey, M. P., Walterscheid, R. L., & Schubert, G. (2015). A full-wave model for a binary gas thermosphere: Effects of thermal conductivity and viscosity. *Journal of Geophysical Research: Space Physics*, 120, 3074–3083. <https://doi.org/10.1002/2014JA020583>

Liu, H.-L. (2017). Large wind shears and their implications for diffusion in regions with enhanced static stability: The mesopause and the tropopause. *Journal of Geophysical Research: Atmospheres*, 122, 9579–9590. <https://doi.org/10.1002/2017JD026748>

Liu, H.-L., McInerney, J. M., Santos, S., Lauritzen, P. H., Taylor, M. A., & Pedatella, N. M. (2014). Gravity waves simulated by high-resolution whole atmosphere community climate model. *Geophysical Research Letters*, 41, 9106–9112. <https://doi.org/10.1002/2014GL024688>

Maute, A. (2017). Thermosphere-ionosphere-electrodynamics general circulation model for the ionospheric connection explorer: TIEGCM-ICON. *Space Science Reviews*, 212(1–2), 523–551. <https://doi.org/10.1007/s11214-017-0330-3>

Mayr, H. G., Talaat, E. R., & Wolven, B. C. (2013). Global propagation of gravity waves generated with the whole atmosphere transfer function model. *Journal of Atmospheric and Solar-Terrestrial Physics*, 104, 7–17. <https://doi.org/10.1016/j.jastp.2013.08.001>

Park, J., Lühr, H., Lee, C., Kim, Y. H., Jee, G., & Kim, J.-H. (2014). A climatology of medium-scale gravity wave activity in the midlatitude/low-latitude daytime upper thermosphere as observed by CHAMP. *Journal of Geophysical Research: Space Physics*, 119, 2187–2196. <https://doi.org/10.1002/2013JA019705>

Plougonven, R., & Zhang, F. (2014). Internal gravity waves from atmospheric jets and fronts. *Reviews of Geophysics*, 52, 33–76. <https://doi.org/10.1002/2012RG000419>

Preusse, P., Dörnbrack, A., Eckermann, S. D., Riese, M., Schaeler, B., Bacmeister, J. T., et al. (2002). Space-based measurements of stratospheric mountain waves by CRISTA 1. Sensitivity, analysis method, and a case study. *Journal of Geophysical Research*, 107(D23), 8178. <https://doi.org/10.1029/2001JD000699>

Richmond, A. D. (1978). Gravity wave generation, propagation, and dissipation in the thermosphere. *Journal of Geophysical Research*, 83(A9), 4131–4145. <https://doi.org/10.1029/JA083iA09p04131>

Simmons, A. J., & Burridge, D. M. (1981). An energy and angular-momentum conserving vertical finite-difference scheme and hybrid vertical coordinates. *Monthly Weather Review*, 109, 758–766. [https://doi.org/10.1175/1520-0493\(1981\)109<0758:AEAAMC>2.0.CO;2](https://doi.org/10.1175/1520-0493(1981)109<0758:AEAAMC>2.0.CO;2)

Smith, A. K. (2012). Global dynamics of the MLT. *Survey of Geophysics*, 33(6), 1177–1230. <https://doi.org/10.1007/s10712-012-9196-9>

Solomon, S. C. (2017). Global modeling of thermospheric airglow in the far ultraviolet. *Journal of Geophysical Research: Space Physics*, 122, 7834–7848. <https://doi.org/10.1002/2017JA024314>

Strickland, D. J., Meier, R. R., Walterscheid, R. L., Christensen, A. B., Paxton, L. J., Morrison, D., et al. (2004). Quiet-time seasonal behavior of the thermosphere seen in the far ultraviolet dayglow. *Journal of Geophysical Research*, 109, A01302. <https://doi.org/10.1029/2003JA010220>

Thébault, E., Finlay, C. C., Beggan, C. D., Alken, P., Aubert, J., Barrois, O., et al. (2015). International Geomagnetic Reference Field: The 12th generation. *Earth, Planets and Space*, 67(1), 79. <https://doi.org/10.1186/s40623-015-0228-9>

Vadas, S. L. (2007). Horizontal and vertical propagation and dissipation of gravity waves in the thermosphere from lower atmospheric and thermospheric sources. *Journal of Geophysical Research*, 112, A06305. <https://doi.org/10.1029/2006JA011845>

Vadas, S. L. (2013). Compressible F-plane solutions to body forces, heatings, and coolings, and application to the primary and secondary gravity waves generated by a deep convective plume. *Journal of Geophysical Research: Space Physics*, 118, 2377–2397. <https://doi.org/10.1002/jgra.50163>

Vadas, S. L., & Fritts, D. C. (2005). Thermospheric responses to gravity waves: Influences of increasing viscosity and thermal diffusivity. *Journal of Geophysical Research*, 110, D15103. <https://doi.org/10.1029/2004JD005574>

Vadas, S. L., & Fritts, D. C. (2006). Influence of solar variability on gravity wave structure and dissipation in the thermosphere from tropospheric convection. *Journal of Geophysical Research*, 111, A10S12. <https://doi.org/10.1029/2005JA011510>

Vadas, S. L., Fritts, D. C., & Alexander, M. J. (2003). Mechanism for the generation of secondary waves in wave breaking regions. *Journal of Atmospheric Science*, 60, 194–214. [https://doi.org/10.1175/1520-0469\(2003\)060<0194:MFTGOS>2.0.CO;2](https://doi.org/10.1175/1520-0469(2003)060<0194:MFTGOS>2.0.CO;2)

- Vadas, S. L., & Liu, H. (2009). Generation of large-scale gravity waves and neutral winds in the thermosphere from the dissipation of convectively generated gravity waves. *Journal of Geophysical Research*, *114*, A10310. <https://doi.org/10.1029/2009JA014108>
- Vadas, S. L., & Nicolls, M. J. (2009). Temporal evolution of neutral, thermospheric winds and plasma response using PFISR measurements of gravity waves. *Journal of Atmospheric and Solar-Terrestrial Physics*, *71*(6-7), 744–770. <https://doi.org/10.1016/j.jastp.2009.01.011>
- Vadas, S. L., Zhao, J., Chu, X., & Becker, E. (2018). The Excitation of secondary gravity waves from body forces: Theory and observation. *Journal of Geophysical Research: Atmospheres*, *123*. <https://doi.org/10.1029/2017JD027970>
- Vlasov, A., Kauristie, K., de Kamp, M. V., Luntama, J., & Pogoreltsev, A. (2011). A study of traveling ionospheric disturbances and atmospheric gravity waves using EISCAT Svalbard radar IPY-data. *Annales Geophysicae*, *29*(11), 2101–2116. <https://doi.org/10.5194/angeo-29-2101-2011>
- Watanabe, S., & Miyahara, S. (2009). Quantification of the gravity wave forcing of the migrating diurnal tide in a gravity wave-resolving general circulation model. *Journal of Geophysical Research*, *114*, D07110. <https://doi.org/10.1029/2008JD011218>
- Yiğit, E., Aylward, A. D., & Medvedev, A. S. (2008). Parameterization of the effects of vertically propagating gravity waves for thermosphere general circulation models: Sensitivity study. *Journal of Geophysical Research*, *113*, D19106. <https://doi.org/10.1029/2008JD010135>
- Yiğit, E., & Medvedev, A. S. (2010). Internal gravity waves in the thermosphere during low and high solar activity: Simulation study. *Journal of Geophysical Research*, *115*, A00G02. <https://doi.org/10.1029/2009JA015106>
- Yiğit, E., & Medvedev, A. S. (2015). Internal wave coupling processes in Earth's atmosphere. *Advances in Space Research*, *55*(4), 983–1003. <https://doi.org/10.1016/j.asr.2014.11.020>